Controlled In Vivo Swimming of a Swarm of Bacteria-Like Microrobotic Flagella

Ania Servant, Famin Qiu, Mariarosa Mazza, Kostas Kostarelos, and Bradley J. Nelson**

Significant attention has been placed recently on the fabrication of micrometer or sub-micrometer structures whose motion can be directed within liquids, enabling controlled navigation to targeted locations and/or achieving tasks under physiological conditions and environments.[1] The design of such sophisticated "microrobots" could potentially revolutionize many fields of medicine, enabling active drug delivery[2] or microsurgery[3] or their combination.

Manipulation of larger-scale objects (typically of a few centimeters) has been achieved in liquids and tissues.[4] In particular, significant advances have been achieved in the development of robot assisted-colonoscopy and in miniature robots for use in the gastrointestinal (GI) tract.[5] Such robots on a millimeter or sub-millimeter scale would enable new diagnosis and therapeutic procedures that were not possible before as additional locations in the human body become accessible.[6] Reaching equivalent or higher level of control for sub-micrometer devices appears to be a more challenging task. The main reason being that at small length scales motion is governed by viscous forces. Micrometer-scale objects, including most microorganisms such as bacteria, typically move at a low Reynolds number, R_e, which represents the ratio of inertial to viscous forces (for *Escherichia coli* R_e is 10^{-4} and for a human swimmer R_e is 10^5).[7] A micrometer or sub-micrometer object needs to execute a non-reciprocal motion at low Reynolds number in order to be able to "swim" and subsequently to overcome the viscous pulling forces.[8] The swimming motion of artificial or tailor made micrometer scale robots will therefore have to be inspired by the natural asymmetric time sequence of microorganisms (screw-like or flexible oar-like movements) such as bacteria or spermatozoa.

Different approaches have been envisioned to mimic the behavior of bacterial and eukaryotic flagella to enable swimming of microrobots such as helical propulsion,[9,10] traveling wave propulsion[11] or pulling with magnetic field gradients.[12] If a micro- and nanoparticle exhibits a chiral geometry such as a helical shape rather than a symmetrical shape, then a non-reciprocal motion can be generated. This concept has been used for helical propulsion-based swimming. The fabrication of such helical microstructures was reported by several research groups using different techniques, such as glancing-angle deposition[13] and self-rolling technology.[14–16] In previous studies, we designed a chiral microstructure displaying the helical geometry of bacterial flagella using direct laser writing (DLW) with two-photon polymerization[17] and photosensitive polymers.[18,19] By coating this polymeric helix with magnetic materials, a stable magnetic structure that exhibited a similar size and geometry to bacterial flagella and capable of controlled "swimming" by magnetic actuation was generated. The application of a temporally constant and rotating magnetic field at appropriate frequencies on these microstructures allowed indeed stable dynamic motion to be produced along the longitudinal axis of the helix and propulsion occurred.[18] These magnetic helical structures, called artificial bacterial flagella (ABFs), could be precisely controlled by weak-strength rotating magnetic fields (<10 mT), that has great potential for biomedical applications, such as targeted drug delivery.[6,7,20]

In our previous work, the functionalization of ABFs with liposomes containing fluorophores and drug models was achieved and a cargo could be delivered in vitro to cells[21,22] to demonstrate the possibility of using ABFs as active drug delivery devices. In this work, we describe the surface functionalization of ABFs with near-infrared probes (NIR-797) that allowed whole-body optical (fluorescence) imaging to track for the first time in vivo the magnetically controlled navigation of a swarm of functionalized ABFs (*f*-ABFs) in the peritoneal cavity of a mouse.

The production of ABFs was optimized by designing a microstructure with the helical geometry of bacterial flagella combining 3D-DLW with two-photon polymerization[17] and photosensitive polymers.[18] By coating this polymeric helix with magnetic materials, stable magnetic structures that exhibit a similar size and geometry to bacterial flagella were successfully prepared. The rotation of temporally constant magnetic field at appropriate frequencies allowed the generation of stable dynamic motion along the longitudinal axis of the helix and consequently allowed propulsion to occur. **Figure 1**A shows the fabricated ABFs. The helical bodies of ABFs could be obtained in different sizes, such as 8 μm (Figure 1A(a)) and 16 μm (Figure 1A(b)) in length. Following DLW, the polymeric bodies were coated with 50 nm-thick layer of Ni and 5 nm layer of Ti. Magnetic material such as Ni enabled us to wirelessly control ABFs, and Ti was used to improve the biocompatibility of the

Dr. A. Servant, Dr. M. Mazza, Prof. K. Kostarelos
Nanomedicine Lab
Faculty of Medical & Human Sciences
and National Graphene Institute
University of Manchester
AV Hill Building, Manchester M13 9PT, UK
E-mail: kostas.kostarelos@manchester.ac.uk
Dr. A. Servant, Dr. M. Mazza, Prof. K. Kostarelos
UCL Faculty of Life Sciences
University College London
Brunswick Square
London WC1N 1AX, UK
F. Qiu, Prof. B. J. Nelson
Institute of Robotics and Intelligent Systems
ETH Zurich
Zurich CH-8092, Switzerland
E-mail: bnelson@ethz.ch

DOI: 10.1002/adma.201404444

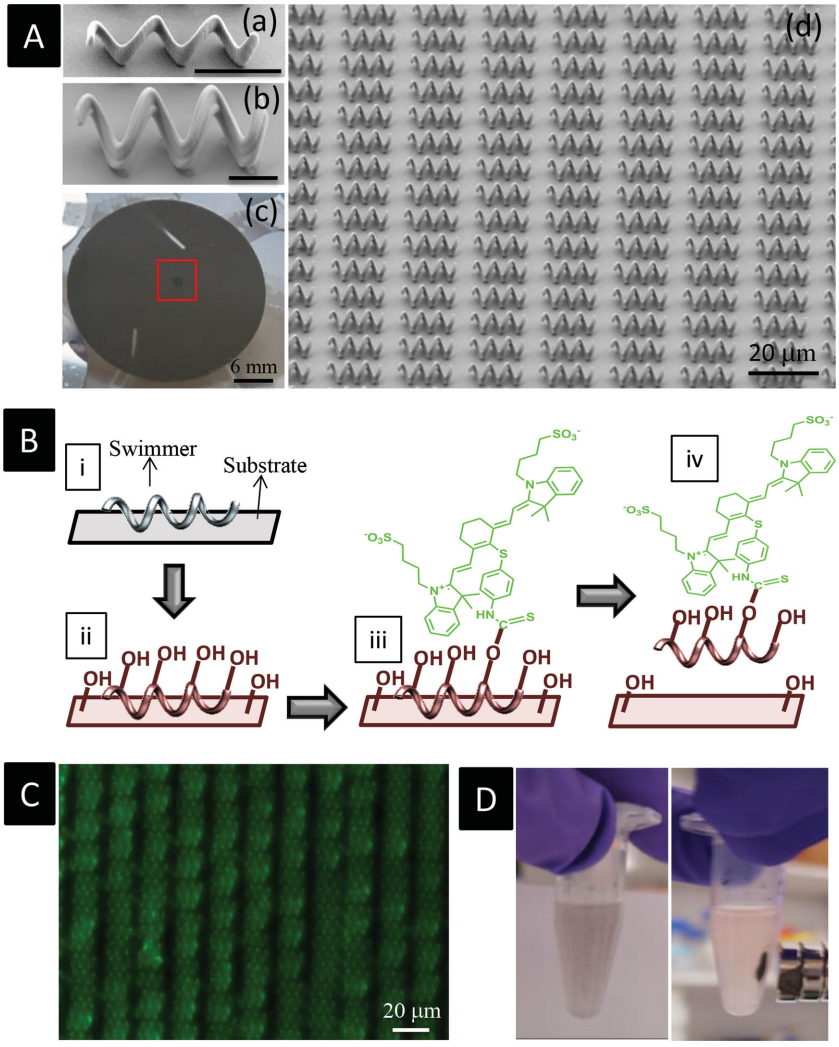

Figure 1. Fabrication of ABFs and their functionalization with NIR-797 dyes (*f*-ABFs). A) ABFs with different lengths (8 µm (a) and 16 µm (b)) were fabricated by DLW, scale bars 4 µm; c) one array of ABFs with 16 µm length (10 080 ABFs) were produced on the glass substrate (dark square inside the red box). B) Functionalization of ABFs with NIR-797 dyes. i) After fabrication, ii) the Ni/Ti surfaces of ABFs were anodized, and iii) covalently coupled with NIR-797 dyes. (iv) After functionalization, the *f*-ABFs were detached from the substrate by sonication. C) The fluorescent image of *f*-ABFs after functionalization. D) The *f*-ABF suspension in a centrifuge tube (left) and near (right) a permanent magnet (500 mT).

devices.[19,23] A large number of ABFs (10 080 in each batch) was produced on a glass slide that served as a substrate and subsequently coated with a Ni/Ti layer (Figure 1A(c)).

Fluorescence-based in vivo imaging in the near-infrared (NIR) spectral region has proven to be a beneficial tool for the development of novel delivery vectors and in particular for monitoring drug targeting. This technique offers the possibility to image agents with higher signal-to-background ratio, and able for deep tissue penetration as a result of the low photon absorption of endogenous biomolecules in the range of 650–1000 nm wavelength.[24] NIR-797 was selected as a NIR-emitting fluorophore in order to monitor the magnetically controlled in vivo navigation of the ABFs using whole-body optical (fluorescence) imaging (IVIS system). The ABFs were functionalized with NIR-797 prior to untethering from the glass substrate in a three-step procedure: i) formation of an oxide layer; ii) derivatization of the hydroxyl groups into amino groups; and iii) coupling with NIR-797 molecule via the reaction between isothiocyanate groups present in NIR-797 molecule and the amino groups on the ABF surface (Figure 1B,C).

The first step that is the formation of a titanium oxide layer was performed by the anodization process. This method has commonly been used to produce a Ti-rich oxide layer on surfaces of super-elastic NiTi alloys for biomedical applications in order to improve corrosion resistance of NiTi-coated materials in physiological environments.[25] In our case, the formation of an oxide layer by anodization was used for the introduction of hydroxyl groups to facilitate the coupling with NIR-797 molecules onto ABF surfaces while leaving the Ni atoms, responsible for the magnetic properties of the swimmers, unaffected. A cross-section of the Ni/Ti-coated glass slide before and after the anodization process is shown on **Figure 2**A. The thickness of the titanium oxide layer could be roughly estimated at 120 ± 30 nm by measuring the difference in thickness before and after anodization with ImageJ using four different samples.

The atom composition of the ABF surface substrate before and after anodization was characterized using energy-dispersive X-ray spectrometry (EDS) (Figure 2B) using an uncoated glass slide as a control. The data confirmed the presence of Ni/Ti atoms on the coated substrates and on the anodized surfaces. The presence of oxygen, aluminum, sodium, potassium, and silane in high proportion could be observed on all samples. These atoms are indeed characteristic of atoms present on a glass slide. The atomic percentage content of oxygen, titanium, and nickel atoms on the surface of the different samples, normalized to the control glass substrate, are shown on Figure 2C to indicate that oxygen content significantly increased after the anodization step, while the one of titanium and nickel remained stable, confirming the formation of the TiO_2 layer on the coated glass substrate.

The addition of reactive amine groups onto the coated ABF surface for the subsequent reaction with the isothiocyanate NIR-797 was performed by introduction of an aminosilane layer. This method was previously reported by Bakhshi et al., in order to coat a polyhedral oligomeric silsesquioxane (POSS)–nanocomposite polymer onto NiTi surfaces.[26] The functionalization of the ABF surface with the aminosilane was found to be highly reproducible and the loading of primary amine groups was around 0.94 nmol cm^{-2} (SD 0.08 nmol cm^{-2}) and considering the surface area of a single ABF

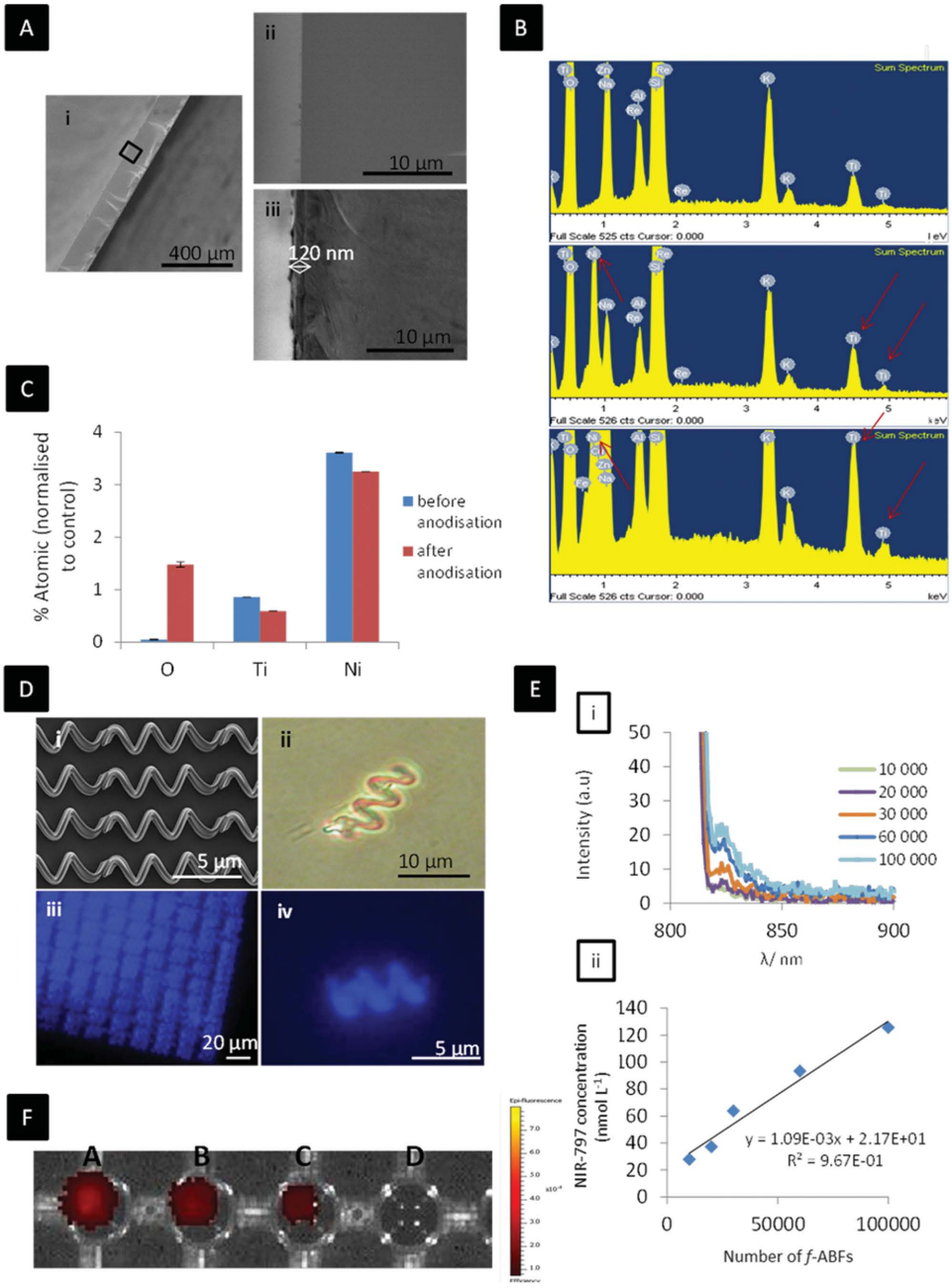

Figure 2. *f*-ABFs characterization; A) Thickness of the titanium oxide (TiO_2) layer after anodization of a Ni/Ti-coated array of ABFs on a glass substrate. i) Scanning electron microscopy (SEM) image of a cross-section of a Ni/Ti-coated glass substrate. Thickness of a Ni/Ti coated glass substrate ii) before anodization and iii) after anodization. The thickness of the oxide layer could be estimated by measuring the difference in thickness between anodized sample and a sample before anodization on four different images using ImageJ software. B) EDS Spectra of i) glass substrate, ii) Ni/Ti-coated glass substrate, and iii) anodized Ni/Ti-coated glass substrate. The red arrows highlight the presence of titanium and nickel on the coated glass substrate. No nickel is detectable on the uncoated glass substrate, however silane, oxygen and aluminum could be detected in every sample as they are component elements of the glass substrate. C) The comparison of elements (O, Ti and Ni) on glass substrates before and after anodization. D) i) SEM images of coated ABFs and ii) optical microscopy image of an untethered coated ABF before functionalization. Epifluorescent images of iii) FITC-functionalized ABFs and iv) untethered FITC-functionalized ABF. E) Characterization of *f*-ABF fluorescence: i) fluorescence signal at 820 nm of *f*-ABFs dispersed in IPA at increasing concentrations (10 000; 20 000; 30 000; 60 000 and 100 000 *f*-ABFs mL^{-1}) (λ_{exc}: 795 nm); ii) Calibration curve of *f*-ABFs dispersed in IPA. The volume of the tested samples was 10 mL. F) The IVIS fluorescence signal of the *f*-ABFs at different concentrations in IPA (60 000; 30 000; 15 000 *f*-ABFs mL^{-1}). A fluorescent signal could be detected at a minimum concentration of 15 000 *f*-ABFs mL^{-1}.

(251.33 μm^2), the functionalization was found to be around 2.36×10^{-7} nmol/ABF (1 amine group per 17.7 $Å^2$) (Figure S1, Supporting Information).

Following this step, the coupling with NIR-797 isothiocyanate was performed at room temperature for 2 d in chloroform/methanol (50/50 vol%). A control reaction was conducted

under the same conditions using a fluorescent isothiocyanate (FITC) (λ_{exc} = 488 nm and λ_{em} = 568 nm) that allowed the observation of fluorescently labeled ABFs under an epifluorescent microscope. The resulting FITC-functionalized ABF surfaces were characterized by fluorescence microscopy and the images are shown in Figure 2D(iii). The data demonstrated a homogenous fluorescence labelling of the functionalized ABF surfaces. The fluorescent signal of the dispersed FITC/NIR-797 functionalized ABFs was characterized by spectro-fluorimetry and fluorescence microscopy (Figure 2D(iv)). In order to quantify the reaction yield of the coupling with NIR-797, a calibration curve was generated using different *f*-ABF concentrations in isopropyl alcohol (IPA) (Figure 2E). The amount of NIR-797 on each *f*-ABF could be estimated and was found to be 1.09×10^{-5} nmol per *f*-ABF. The yield of the NIR-797/NH_2-functionalized ABF coupling reaction was therefore around 5%. This low yield was explained by the fact the NIR-797 is a bulky molecule with limited accessibility to the amino groups located on the surface of the ABF.

The fluorescent signal of the NIR-797/ABF coupling was then studied in aqueous and physiological media such as HEPES buffer (25×10^{-3} M, pH 7.4), 5% dextrose, and mouse serum (Figure S2A, Supporting Information). The intensity of the fluorescent signal of the *f*-ABFs varied in the different solvent systems (Figure S2B, Supporting Information), this was consistent with the extinction coefficient of NIR-797 in the same solvents. NIR-797 extinction coefficient was found to be higher in mouse serum than in all the other solvents. Mouse serum appeared to be the best solvent for an optimal NIR-797 fluorescent signal. The stability of the fluorescent signal of the *f*-ABFs in 5% dextrose and 50% mouse serum was also studied overtime (Figure S2C, Supporting Information). The fluorescent signal remained unchanged over a period of 2 weeks in all media used.

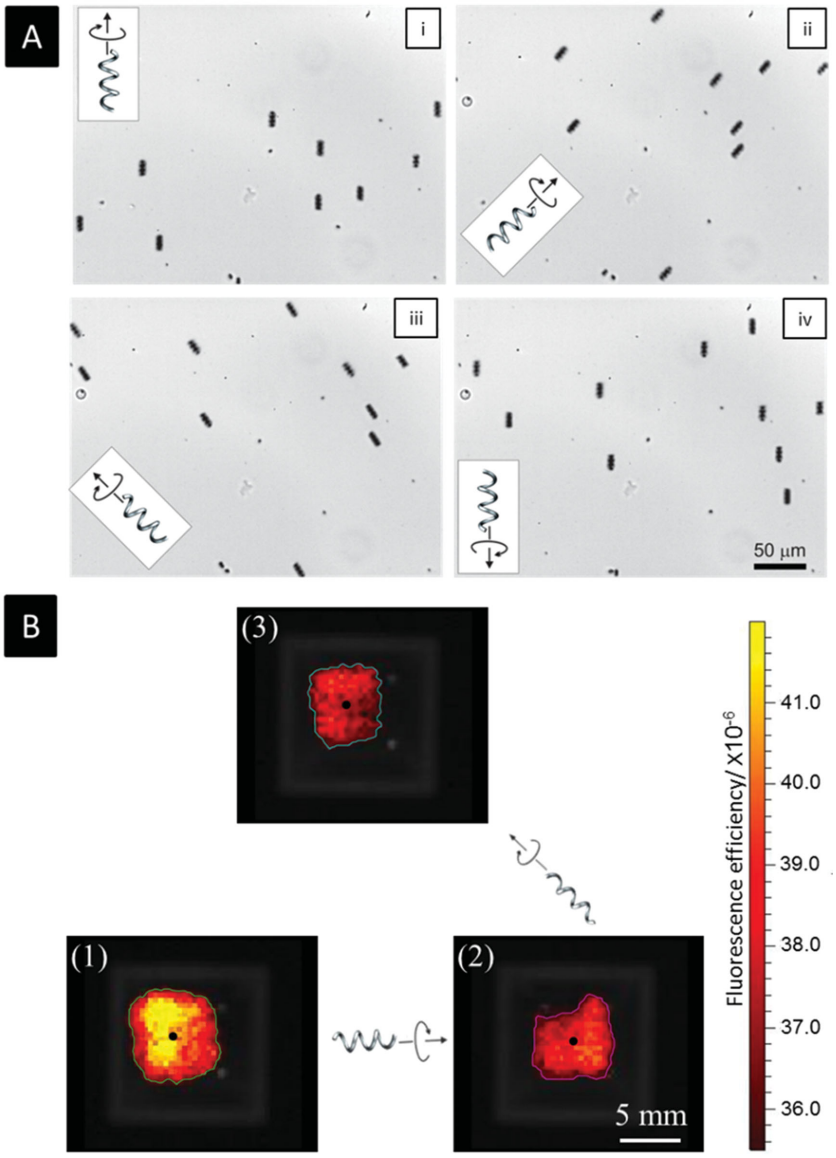

Figure 3. Controlled swimming of *f*-ABF swarm in vitro under 9 mT and 90 Hz. A) A swarm of ABFs swims on a polished Si wafer in distilled water tracked by optical microscopy. B) A swarm of ABFs swims in a 1 cm × 1 cm vial tracked by the IVIS Lumina III and Live Imaging software. The colored lines around the clouds present the contours of the clouds, measured by Icy software and the "●" symbol indicates the centroids of the clouds.

In order to investigate the swimming ability of the *f*-ABFs, the intensity of the NIR fluorescent signal was determined using the IVIS optical imaging system at an excitation wavelength of 745 nm, at which the absorption of endogenous biomolecules is expected to be low. *f*-ABFs were dispersed in 5% dextrose at different concentrations (60 000, 30 000, and 15 000 *f*-ABFs mL^{-1}) were prepared and the fluorescent signal was investigated. The results are shown in Figure 2F. The fluorescent signal decreased with decreasing the number of *f*-ABFs, and a fluorescent signal could be detected with a concentration of *f*-ABFs as low as 15 000 *f*-ABFs mL^{-1}.

The *f*-ABFs in vitro swimming capabilities by wireless magnetic actuation were then investigated. **Figure 3**A and Movie S1 and S2 in the Supporting Information show the controlled motion of a *f*-ABF swarm (of around 20 000 ABFs) observed by optical microscopy using three pairs of Helmholtz coils that provided a rotational magnetic field (Figure S3, Supporting Information). The application of a rotational magnetic field allowed the *f*-ABFs to translate a rotational movement into propulsion (Figure S4A, Supporting Information).[27] Since the intensity of the magnetic field inside the coil was uniform, the whole swarm of *f*-ABF movement could be precisely controlled. Depending on the input magnetic fields, ABFs can assemble and disassemble. The assembly between two ABFs can alter the swimming speed depending on the angle of assembly. When this event occurs, as was previously demonstrated in our group,

the assembled ABFs are still able move in a same direction and the swimming can still be controlled.[28]

Altering the rotating magnetic field parameters such as field strength and frequency allowed the tuning and control of the swimming direction and speed of the swarm. Yaw and pitch were the steering parameters in order to control the orientation of the ABFs in the horizontal plane and out-of-plane, respectively. In addition, the *f*-ABFs could swim with six degrees of freedom (left, right, forward, backward, up, down, and free rotation about three perpendicular axes).[27] When ABFs swim on an in-plane surface, they have both forward and drift speeds due to the drag force imbalance of the wall effect. In order to reduce the drift speed, the swimming experiments were conducted at 10° out-of-plane (pitch 10). The average speed of the *f*-ABFs was 70.4 μm s^{-1} (the forward speed 69.1 μm s^{-1} and the drift speed 13.3 μm s^{-1}) under a magnetic field of 9 mT and 90 Hz (Figure S4B, Supporting Information).

The swimming of *f*-ABF swarms was then studied by IVIS optical imaging. 120 000 ABFs were suspended in a total volume of 1 cm^3 (with a calculated mean spacing for that ABF suspension of 184 μm between each swimmer). Mild sonication was applied prior to all swimming experiments. Figure 3B shows the controlled motion of a *f*-ABF swarm (about 110 000 ABFs dispersed in 1 mL of 5% dextrose) in a 1 cm × 1 cm quartz cuvette. The three Helmholtz coils were placed inside the IVIS chamber under the camera to allow direct visualization of the *f*-ABF swarm swimming. The fluorescence signal generated by the *f*-ABF dispersion in 5% dextrose appeared as a red cloud in the IVIS images (Figure 3B) and indicated the location and distribution of the *f*-ABF swarm. The rotation of the magnetic field was programmed for a precise trajectory: from their initial position, the *f*-ABF swarm was exposed to a rotating magnetic for a propelling motion to the right (9 mT, 90 Hz, yaw 90, pitch 10, 1 min exposure time) (Figure 3B(1),(2)), then the direction of the rotating magnetic field was changed for a propelling motion to a diagonal direction toward the upper left corner of the quartz cell (9 mT, 90 Hz, 1 min exposure time) (Figure 3B(3)). Images of the *f*-ABF swarm before application of the field were first recorded, and then every minute after application of the field.

The swimming pattern of the *f*-ABF swarm was demonstrated by the changing shape of the cloud. In order to statistically study the movement of the swarm, the movement of the centroid of the cloud was studied and quantified using Icy software 1.4.3.5 to determine the centroid position by an active contour function and a home-made Matlab code (Figure S5, Supporting Information). The centroid moved 1182 μm toward the right from (1) to (2) with a total speed of 19.7 μm s^{-1} (forward speed 18.5 μm s^{-1}, drift speed 6.8 μm s^{-1}) (Figure S5A, Supporting Information). Afterwards, the centroid appeared to be displaced to 1102 μm diagonally, toward the upper left corner from (2) to (3) (at total speed of 18.3 μm s^{-1}, forward speed 18.0 μm s^{-1}, and drift speed 3.6 μm s^{-1}) (Figure S5B, Supporting Information). The movement of the cloud centroid was found to be consistent with the actuation trajectory. Both the optical (Figure 3A) and IVIS tracking (Figure 3B) showed that the swarm of *f*-ABFs exhibited controlled motion by actuation of the rotational magnetic field. The speed of movement of the centroid in 5% dextrose was found to be slower than the speed measured in IPA in Figure 3A. This could be explained by possible aggregation of the *f*-ABFs due to their surface modification, change of media from IPA to an aqueous medium and the magnetic attraction between *f*-ABFs. When aggregated, the ABFs were still able to move forward, however their speed decreases as previously described.[28]

We then investigated the controlled propelling of the *f*-ABF swarm in vivo. A swarm of *f*-ABFs dispersed in 5% dextrose (80 000 *f*-ABFs in 400 μL) was injected in the intra-peritoneal cavity of a 4-week old Balb/C mouse. All in vivo experiments described in this work were performed in accordance and approval by the UK Home Office (Animal Scientific Procedures Act 1986, UK) and all Ethical Review Committees that oversee such work. The peritoneal cavity is the space between the parietal peritoneum and visceral peritoneum[29] and was selected as a site of injection that would allow enough space for navigation of the swimming *f*-ABFs. Immediately after injection, the animals were anesthetized and placed upside down with the lower abdominal part located at the center of the three pairs of the Helmholtz coils (**Figure 4**A(i)). This experimental setup is shown in Figure S6A (Supporting Information). A fluorescent signal could be detected in the lower part of the abdominal cavity consistent with the location of the injected *f*-ABFs (Figure 4A(ii)). Intraperitoneal administration with a 5% dextrose solution showed no background fluorescent signal with the optical setup used, confirming that the fluorescent signals detected originated from the swarm of *f*-ABF (Figure S6B, Supporting Information). A rotational magnetic field was applied (9 mT, 90 Hz, yaw 0, and pitch 10) for 5 min to induce a propelling actuation of the *f*-ABFs at a direction toward the lower part of the animal body. Images were captured every minute. As shown in Figure 4B, the *f*-ABF swarm represented by the red and yellow cloud appeared to move toward the direction of the magnetic field overtime. This suggested that the *f*-ABFs responded to the rotational magnetic field and could swim within the intraperitoneal cavity. Similar to the in vitro studies, the location of the *f*-ABFs cloud centroid was monitored and quantified (Figure S7, Supporting Information). The downward motion of the cloud centroid was estimated to be 1.25 mm after 5 min of field exposure and the speed of the cloud was found to be 6.8 μm s^{-1} (forward speed 4.2 μm s^{-1} and drift speed 5.4 μm s^{-1}) which was slower than the speed measured in the in vitro studies. The decreased speed of the propelling *f*-ABF motion can be explained by increased fluid viscosity, the change of surface properties of *f*-ABFs, the shift of the step-out frequency of *f*-ABFs and the change of the effective hydrodynamic pitch of ABFs inside the intraperitoneal cavity due to the presence of proteins and other endogenous bio-macromolecules. Also, the tissue in vivo presents various anatomical barriers to *f*-ABF swimming that will also be another reason for the reduced speed of the in vivo swimming observed.

Another explanation of the reduction of the swimming speed is that during the in vitro experiments under the optical microscope, the ABFs operated at the step-out frequency. At that frequency they reached their maximum swimming speed. For the in vitro and in vivo experiments in biological media, this remains unclear as the step-out frequency was determined in water or IPA. As a consequence the *f*-ABFs may operate below the step-out frequency. In addition to the technical challenge

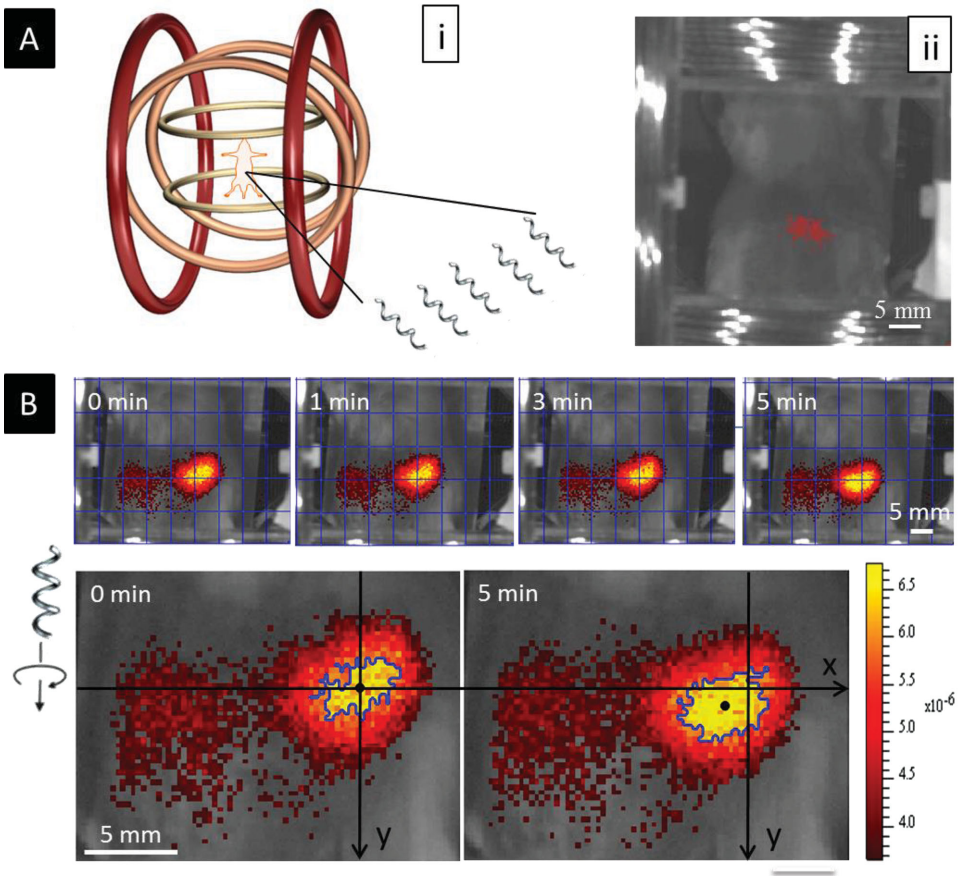

Figure 4. Controlled swimming of a swarm of *f*-ABFs in the intra peritoneal cavity of a Balb-C mouse under 9 mT and 90 Hz. A) The scheme of the in vivo experiment (i) and the original data taken by the IVIS Lumina III using Live Imaging software; ii) Image of an anesthetized 4 week old Balb-C mouse inside the magnetic coils. The red spots represent the fluorescent signal of the injected *f*-ABFs. B) A swarm of *f*-ABFs (80 000 *f*-ABFs in 400 µL) swimming downward under the actuation of a rotating magnetic field (9 mT, 90 Hz). The upper array of three images shows the swarm of *f*-ABFs swimming downwards (total movement of the swarm center of mass: 1.3 mm) and the bottom images are the magnified image from the upper array. The contour of the yellow cloud was determined using a homemade Matlab code and was used to determine the movement of the swarm of *f*-ABFs.

of navigating this type of swimmers in an in vivo environment (within tissues and organs as potential obstacles) using a rotating magnetic field, another technical issue had to be considered carefully such as the development of a suitable imaging technology that could allow monitoring of actuation of such small-sized devices by wireless actuation. The right balance between the number of swimmers that could allow strong-enough detectable signal to allow monitoring and tracking with preservation of control of their in vivo actuation and navigation needed to be optimized. A high amount of swimmers (80 000) were required in order to obtain a sufficient signal that allow accurate in vivo tracking increasing the possibility of movement impairment of the swimmers and therefore significant reduction of the swimming speed.

Recent interest has focused on the design and utilization of magnetically propelled constructs to transport therapeutic agents to precisely targeted locations of the body by active navigation, despite this remaining challenging.[30–34] Significant progress has been achieved in manipulating larger scale materials in liquids and tissue. For example, the navigation of a 1 cm ferromagnetic screw in tissue with a rotating magnetic field, as well as the navigation of a 1.5 mm bead in the carotid artery using magnetic field gradients were reported.[35,36] The use of the magnetic field as an external source of power for microswimmers is the common route for powering swimming motion as magnetic fields are known to be less invasive than other forms of actuation. In addition, the utilization of magnetic fields in medicine and in biological environments is well accepted as the widespread use of magnetic resonance imaging (MRI) can demonstrate. One of the approaches to navigate magnetic micro- and nano-particles is to use external magnetic field gradients to provide a translational motion. However, an important consideration when utilizing magnetic field gradients to be taken into account is the system scale size. It has been demonstrated that producing a magnetic field gradient to propel objects over long distances, typically required for in vivo applications, becomes unattainable when considering the capabilities of available sources of magnetic fields.[37]

Another approach to achieve navigation of magnetic micro- and nanoparticles using magnetic fields is based on the exploitation of the mechanism of traveling wave propulsion. This method of navigation relies on the creation of a traveling

wave to generate propulsion the same way as that of eukaryotic flagella.[38] This method is found to be a very effective means of propulsion, possibly more effective than helical propulsion. However, the development of such systems in terms of fabrication, power, and control appears to be challenging with regards to the type of distributed actuation seen in eukaryotic flagella.[6] The advantage of using helical and screw-like structures, as in the case of ABFs, is their ability to operate with the application of a weak (<10 mT) and homogenous external magnetic field. At such field intensities spherical or symmetrical ferromagnetic nanoparticles cannot be propelled, nor be dragged. When the magnetic field rotates in a plane orthogonal to the main axis of the helix, the ABF rotate and as a result a propelling motion is achieved (similar to a screw turning), going forward or backward depending on the direction of rotation of the field.[8]

Various microrobot designs, using different forms of actuation have been reported to swim in vitro in physiological environments.[39–44] Magnetically actuated micro- and nanoswimmers have been studies in biological fluids such as fetal bovine serum,[28] human serum,[45] undiluted human blood[46] and saliva.[47] In addition, our previously published work demonstrated that use of a Ni/Ti coating on the ABFs were not found to induce any cytotoxicity to mouse myoblasts (C2C12) after 72 h of exposure, or HEK293 cells within 96 h of exposure. The cells readily adhered, migrated and proliferated over the devices.[18,23] However, the present study reports previously unattained in vivo navigation of a swarm of microscale, magnetically-actuated swimmers. The "swimming" motion of the surface-functionalized ABFs as a result of the application of a mild external rotating magnetic field in the peritoneal cavity of an anesthetized mouse could be tracked and monitored in real time using live fluorescence imaging. The anticipated dilution effect and fluid absorption by the tissue following injection, along with the interaction with proteins and other biomolecules present in the peritoneal cavity represent significant obstacles for the smooth navigation of the ABFs compared to an in vitro environment. There has been no prior knowledge or report on how such micro-objects would react in a living physiological environment. For many applications, as well as being able to potentially retrieve the swimmers, the ability to visualize and monitor the "swimming" motion of microrobots will be essential. This study demonstrates the ability to navigate these microrobots in an in vivo set-up that has not been previously achieved. However, for the translation of this technology in clinical applications there are still important challenges to be addressed, such as: i) the ABF surface interaction with biomolecules and their impact on their swimming properties; ii) the number of ABFs to be used in a swarm for optimal delivery of drugs to a targeted site; and iii) a thorough investigation of the ABF in vivo toxicity in order to fully understand any long-term effects on the interacting tissue and the excretion mechanism of the swimmers after accomplishment of their navigation mission.

Non-optical methods, such MRI, have been found to be useful, in particular combined with paramagnetic and ferromagnetic microparticles that enhance the MRI signal contrast. However, MRI becomes unfeasible because high magnetic fields, typically associated with MRI instrumentation, will interfere with the magnetization of the ABF swimmers, particularly in ferromagnetic systems actuated with homogenous magnetic fields.[48] In this case, there is a need to incorporate alternative imaging signals to enable tracking and visualization. Here we demonstrated that the chemical functionalization of the ABFs with a NIR fluorophore, NIR-797, provides adequate imaging to allow tracking of the *f*-ABF swarm trajectory in the body of the animal. Although the speed of the *f*-ABF swimming motion was found to be lower in vivo than in vitro, the 3D directionality of the *f*-ABF swarm actuation could still be achieved. This represents a significant progress for the development of microscale robots that could be navigated, imaged and tracked in vivo that could constitute a technology platform for advanced, wirelessly controlled and imaged vehicles for transport of therapeutics and tools for microsurgery.

Supporting Information

Supporting Information is available from the Wiley Online Library or from the author.

Acknowledgements

A.S. and F.Q. contributed equally to this work. The authors thank Kathrin E. Peyer and Soichiro Tottori from ETH Zurich and Prof. Li Zhang of the Chinese University of Hong Kong for their valuable discussions. The authors would also like to thank Roel Pieters and Franziska Ullrich for their help with the Matlab codes for the in vivo data analyses. They would also like to than Dr. Alan Parish for his help with the SEM-EDS measurements. The authors thank Yun Ding from ETH Zurich for his support of the microwell. They are grateful to the FIRST lab at ETH Zurich for technical support. Funding for this research was partially provided by the European Research Council Advanced Grant BOTMED and the Sino-Swiss Science and Technology Cooperation (SSSTC) (Grant No. IZLCZ2_138898) and the United Kingdom Engineering and Physical Sciences Research Council (EPSRC) (Grant No. EP/G061882/1) under the Grand Challenge in Nanotechnology: Healthcare scheme.

Received: September 26, 2014
Revised: February 28, 2015
Published online: April 7, 2015

[1] G. A. Ozin, I. Manners, S. Fournier-Bidoz, A. Arsenault, *Adv. Mater.* **2005**, *17*, 3011.
[2] K. K. Coti, M. E. Belowich, M. Liong, M. W. Ambrogio, Y. A. Lau, H. A. Khatib, J. I. Zink, N. M. Khashab, J. F. Stoddart, *Nanoscale* **2009**, *1*, 16.
[3] R. A. Freitas Jr., *Int. J. Surgery* **2005**, *3*, 243.
[4] A. Menciassi, M. Quirini, P. Dario, *Minimally Invasive Ther. Allied Technol.* **2007**, *16*(2), 91.
[5] I. Kassim, L. Phee, W. S. Ng, G. Feng, P. Dario, C. A. Mosse, *IEEE Eng. Med. Biol. Mag.* **2006**, *25*, 49.
[6] B. J. Nelson, I. K. Kaliakatsos, J. J. Abbott, *Annu. Rev. Biomed. Eng.* **2010**, *12*, 55.
[7] K. E. Peyer, L. Zhang, B. J. Nelson, *Nanoscale* **2013**, *5*, 1259.
[8] P. Fischer, A. Ghosh, *Nanoscale* **2011**, *3*, 557.
[9] T. Honda, K. I. Arai, K. Ishiyama, *IEEE Trans. Magn.* **1996**, *32*, 5085.
[10] A. Ghosh, P. Fischer, *Nano Lett.* **2009**, *9*, 2243.

[11] B. Behkam, M. Sitti, *J. Dyn. Syst., Meas., Control* **2005**, *128*, 36.
[12] G. T. Gillies, R. C. Ritter, W. C. Broaddus, M. S. Grady, M. A. Howard, R. G. McNeil, *Rev. Sci. Instrum.* **1994**, *65*, 533.
[13] K. Robbie, M. J. Brett, *J. Vac. Sci. Technol. A* **1997**, *15*, 1460.
[14] L. Zhang, E. Deckhardt, A. Weber, C. Schonenberger, D. Grutzmacher, *Nanotechnology* **2005**, *16*, 655.
[15] L. Zhang, J. J. Abbott, L. X. Dong, B. E. Kratochvil, D. Bell, B. J. Nelson, *Appl. Phys. Lett.* **2009**, *94*, 064107.
[16] S. Schuerle, S. Pane, E. Pellicer, J. Sort, M. D. Baro, B. J. Nelson, *Small* **2012**, *8*, 1498.
[17] S. Kawata, H. B. Sun, T. Tanaka, K. Takada, *Nature* **2001**, *412*, 697.
[18] S. Tottori, L. Zhang, F. M. Qiu, K. K. Krawczyk, A. Franco-Obregon, B. J. Nelson, *Adv. Mater.* **2012**, *24*, 811.
[19] F. Qiu, L. Zhang, K. E. Peyer, M. Casarosa, A. Franco-Obregon, H. Choi, B. J. Nelson, *J. Mater. Chem. B* **2014**, *2*, 357.
[20] K. E. Peyer, S. Tottori, F. Qiu, L. Zhang, B. J. Nelson, *Chem. Eur. J.* **2013**, *19*, 28.
[21] F. Qiu, R. Mhanna, L. Zhang, Y. Ding, S. Fujita, B. J. Nelson, *Sens. Actuators, B* **2014**, *196*, 676.
[22] R. Mhanna, F. Qiu, L. Zhang, Y. Ding, K. Sugihara, M. Zenobi-Wong, B. J. Nelson, *Small* **2014**, *10*, 1953.
[23] S. Kim, F. Qiu, S. Kim, A. Ghanbari, C. Moon, L. Zhang, B. J. Nelson, H. Choi, *Adv. Mater.* **2013**, *25*, 5863.
[24] S. A. Hilderbrand, R. Weissleder, *Curr. Opin. Chem. Biol.* **2010**, *14*, 71.
[25] A. Michiardi, C. Aparicio, J. A. Planell, F. J. Gil, *J. Biomed. Mater. Res., Part B* **2006**, *77B*, 249.
[26] R. Bakhshi, A. Darbyshire, J. E. Evans, Z. You, J. Lu, A. M. Seifalian, *Colloids Surf., B* **2011**, *86*, 93.
[27] L. Zhang, K. E. Peyer, B. J. Nelson, *Lab Chip* **2010**, *10*, 2203.
[28] S. Tottori, L. Zhang, K. E. Peyer, B. J. Nelson, *Nano Lett.* **2013**, *13*, 4263.
[29] P. Tank, in *Grant's Dissector*, 15th ed., LWW, Philadephia, PA, USA **2012**, p. 99.
[30] A. Ito, M. Shinkai, H. Honda, T. Kobayashi, *J. Biosci. Bioeng.* **2005**, *100*, 1.
[31] Q. A. Pankhurst, N. T. K. Thanh, S. K. Jones, J. Dobson, *J. Phys. D: Appl. Phys.* **2009**, *42*, 224001.
[32] N. Tran, T. J. Webster, *J. Mater. Chem.* **2010**, *20*, 8760.
[33] R. Tietze, S. Lyer, S. Durr, C. Alexiou, *Nanomedicine* **2012**, *7*, 447.
[34] R. Banerjee, Y. Katsenovich, L. Lagos, M. McIintosh, X. Zhang, C. Z. Li, *Curr. Med. Chem.* **2010**, *17*, 3120.
[35] K. Ishiyama, M. Sendoh, A. Yamazaki, K. I. Arai, *Sens. Actuators, A* **2001**, *91*, 141.
[36] S. Martel, J. B. Mathieu, O. Felfoul, A. Chanu, E. Aboussouan, S. Tamaz, P. Pouponneau, *Appl. Phys. Lett.* **2007**, *90*, 114105.
[37] J. J. Abbott, K. E. Peyer, M. C. Lagomarsino, L. Zhang, L. X. Dong, I. K. Kaliakatsos, B. J. Nelson, *Int. J. Robotics Res.* **2009**, *28*, 1434.
[38] D. M. Woolley, R. F. Crockett, W. D. I. Groom, S. G. Revell, *J. Exp. Biol.* **2009**, *212*, 2215.
[39] O. J. Sul, M. R. Falvo, R. M. Taylor, S. Washburn, R. Superfine, *Appl. Phys. Lett.* **2006**, *89*, 203512.
[40] B. R. Donald, C. G. Levey, C. D. McGray, I. Paprotny, D. Rus, *J. Microelectromech. Syst.* **2006**, *15*, 1.
[41] C. Pawashe, S. Floyd, M. Sitti, *Appl. Phys. Lett.* **2009**, *94*, 164108.
[42] B. Watson, J. Friend, L. Yeo, *J. Micromech. Microeng.* **2009**, *19*, 115018.
[43] S. T. Chang, V. N. Paunov, D. N. Petsev, O. D. Velev, *Nat. Mater.* **2007**, *6*, 235.
[44] Y. Osada, H. Okuzaki, H. Hori, *Nature* **1992**, *355*, 242.
[45] W. Gao, X. M. Peng, A. Pei, C. R. Kane, R. Tam, C. Hennessy, J. Wang, *Nano Lett.* **2014**, *14*, 305.
[46] P. L. Venugopalan, R. Sai, Y. Chandorkar, B. Basu, S. Shivashankar, A. Ghosh, *Nano Lett.* **2014**, *14*, 1968.
[47] V. Garcia-Gradilla, J. Orozco, S. Sattayasamitsathit, F. Soto, F. Kuralay, A. Pourazary, A. Katzenberg, W. Gao, Y. F. Shen, J. Wang, *ACS Nano* **2013**, *7*, 9232.
[48] S. Martel, O. Felfoul, M. Mohammadi, in *2nd IEEE RAS-EMBS Int. Conf. on Biomedical Robotics and Biomechatronics*, IEEE **2008**, p. 264.
[49] W. Haider, N. Munroe, V. Tek, C. Pulletikurthi, P. K. S. Gill, S. Pandya, *J. Long-Term Eff. Med. Implants* **2009**, *19*, 113.
[50] C. Menard-Moyon, C. Fabbro, M. Prato, A. Bianco, *Chem. Eur. J.* **2011**, *17*, 3222.
[51] K.-H. Chuang, H.-E. Wang, F.-M. Chen, S.-C. Tzou, C.-M. Cheng, Y.-C. Chang, W.-L. Tseng, J. Shiea, S.-R. Lin, J.-Y. Wang, B.-M. Chen, S. R. Roffler, T.-L. Cheng, *Mol. Cancer Ther.* **2010**, *9*, 1903.